V$_2$O$_5$ nanodot-decorated laminar C$_3$N$_4$ for sustainable photodegradation of amoxicillin under solar light

Shukun Le [a], Chengzhang Zhu [b,*], Yuwen Cao [c], Peng Wang [a], Quansheng Liu [a], Huacong Zhou [a], Chuanxiang Chen [b], Shaobin Wang [d], Xiaoguang Duan [d,*]

[a] *Chemical Engineering College, Inner Mongolia University of Technology, Huhhot 010051, China*
[b] *School of Environmental and Chemical Engineering, Jiangsu University of Science and Technology, Zhenjiang 212100, China*
[c] *International Genome Center, Department of Immunology, Jiangsu University, Zhenjiang 212013, China*
[d] *School of Chemical Engineering and Advanced Materials, The University of Adelaide, Adelaide, SA 5005, Australia*

ARTICLE INFO

ABSTRACT

Innovative solar-driven heterostructure photocatalysts are promising for removing deleterious antibiotics residues in the water environment. Herein, we prepared a vanadium pentoxide/graphitic carbon nitride (V$_2$O$_5$/C$_3$N$_4$) S-scheme with a facile approach. The heterostructure provides larger surface areas, promotes the separation and transfer of charge carriers, and offers abundant active sites for photocatalytic redox reactions. The composites were used to degrade amoxicillin (AMX) under solar light which attained a high removal efficiency (91.3%) and stability. Meanwhile, the photodegradation pathway of AMX was revealed by HPLC-MS/MS analysis and density functional theory (DFT) computations. Superoxide radicals evolved from conduction band of C$_3$N$_4$ and oxidative holes were generated from valence band of V$_2$O$_5$, which were confirmed by electron spin resonance experiments and selective radical quenching experiments. The V$_2$O$_5$/C$_3$N$_4$ S-scheme structure provides an internal electron channel at the interface and maintains the active sites with high potentials for photodegradation. Our work affords a robust V$_2$O$_5$/C$_3$N$_4$ S-scheme nanocomposites for sustainable water purification.

1. Introduction

Antibiotics are diverse in terms of chemical structure, solubility, toxicity, stability, and antidegradation. As one of β-lactam antibiotics, amoxicillin (AMX) is extensively used in medicine and veterinary medicine [1–3]. AMX has been found in groundwater, surface water and soils, which have caused serious risks, including endocrine disorders and antibiotic resistance in humans [4–7]. Owing to its complex structure, high chemical stability, and good solubility in the water environment, it is challenging to remove AMX from wastewater by traditional wastewater treatment plants. To this end, advanced oxidation processes (AOP) are effective and promising techniques for purifying various aqueous contaminations [8–10], but AOPs are limited by the high cost of intensive chemical inputs and post-treatment. The photocatalysis is a green and energy-saving technology for environmental pollution control. However, the traditional heterojunction photocatalysts cannot simultaneously maintain the high reductive and oxidizing capabilities. For instance, photogenerated e$^-$ and h$^+$ in typical Type I and Type II heterojunctions can be effectively separated but their redox ability declines

[11–13]. Particularly, Type II heterojunctions are appealing in photocatalysis owing to the appropriate band alignment [14]. Unfortunately, Type II heterojunctions system is limited by the expense of reducing redox ability, and the photogenerated electrons (e$^-$) and holes (h$^+$) remain on the individual compounds. Spatial separation of charge carriers cannot be achieved in Type II composites due to electrostatic repulsions between CB(e$^-$) - CB(e$^-$) and/or VB(h$^+$) - VB(h$^+$) [15]. The step-scheme (S-scheme) heterojunctions stand out which combine an oxidizing photocatalyst (OP) and a reductive photocatalyst (RP) with the interlaced band structures enables a lower recombination rate of photogenerated carriers within each component and thus maintain higher redox potentials [16]. In S-scheme heterojunction, the higher photogenerated e$^-$ in the conduct band (CB) of RP and the photogenerated h$^+$ in the valence band (VB) of OP are reserved, while the less reactive carriers (h$^+$ in VB of RP and e$^-$ in CB of OP) are recombined due to the thermodynamic feasibility, resulting in spatial separation of carriers in each individual component and preserve the high redox species (h$^+$ in VB of OP and e$^-$ in CB of RP) [17].

Recently, as a metal-free polymer semiconductor, graphitic carbon

---

nitride (C_3N_4 or GCN) has attracted rising interests in photocatalysis owing to their narrow band gap (about 2.7 eV) and wide range absorbance in the visible region [18–20]. Engineering GCN with different nanoarchitectures can improve the physicochemical characteristics to accelerate the separation of photogenerated carriers and increase the specific surface area (SSA). Therefore, various design strategies of GCN structures have been proposed including zero dimensional (0D) [21], one dimensional (1D) [22], two dimensional (2D) [23], and three dimensional (3D) nanoarchitectures [24]. Recently, ultrathin 2D nanosheets are appealing features for photocatalysts due to plentiful active sites, large SSA, and short diffusion path of photogenerated carriers [25–27]. As a typical structure, 2D GCN has been extensively used as a visible-light-responsive photocatalyst for CO_2 reduction [28], hydrogen evolution [29], and photodegradation [30]. Owing to featured electronic properties and abundant active sites [31], 2D GCN secures efficient transfer of charge carriers and provides extensive surface active sites for photocatalytic reactions. 2D GCN photocatalysts are promising for removal of hazardous organic pollutants due to the proper band edges, low toxicity, favorable photocatalytic performance and chemical/structural robustness [32]. Additionally, the ultrathin 2D nanosheet structure is favorable for establishing heterojunctions with abundant coupling heterointerfaces [33]. Intact 2D structures have great resistance against acid, base, and organic solvents, which is beneficial for practical applications in complicated environments [34]. However, the photocatalytic performance of pure GCN is limited by insufficient solar light absorption and suffers from rapid recombination of photoinduced carriers, leading to low quantum efficiency and photocatalytic activity. Multiple strategies have been proposed to improve the photocatalytic activity of GCN, including surface modification [35], element doping [36], and building heterojunctions [37]. For instance, construction of GCN-based S-scheme heterojunctions with a narrow band gap will provide a facile approach to enhancing photocatalytic activity and utilization of solar light.

Vanadium pentoxide (V_2O_5) is a semiconductor with a layered structure, which have been widely applied as host materials in rechargeable batteries, optoelectronic devices, and gas sensors [38]. V_2O_5 has a distinctive narrow band gap (~2.3 eV), making it responsive to a wide range of solar spectrum [39]. Thus, V_2O_5 is favorable in photocatalysis because of the strong oxidizing capacity and structural stability against chemical and photo-induced decay [40]. Furthermore, V_2O_5 has proper band edges, which may match well with C_3N_4 to establish S-scheme heterojunctions.

In this investigation, the S-scheme heterojunction nanocomposites were synthesized through coupling V_2O_5 with ultrathin V_2O_5 nanosheets via a facile heat treatment strategy. In this S-scheme photocatalytic system, the photogenerated e^- in CB of C_3N_4 displays powerful reducibility and the photogenerated h^+ in VB of V_2O_5 show strong oxidation capacity. Meanwhile the low reactive charge carriers are recombined at the interface to enhance the separation of photogenerated carriers in each component and reserve strong redox species. Then the materials were applied to degrade aqueous AMX under solar light irradiation. The operational factors such as photocatalyst dosage, AMX concentration, and pH value were investigated. Furthermore, the S-scheme induced enhanced photocatalysis was proposed for AMX degradation. This work affords an effective strategy for removing antibiotics in water based on high-performance S-scheme photocatalysts with solar light response.

2. Experimental

2.1. Chemicals and materials

All chemical reagents utilized in this study are analytical grade without further purification. The water used is deionized from laboratory preparation. The characteristic and CAS number of the chemical reagents are listed in Table S1.

2.2. Synthesis of V_2O_5/C_3N_4

The fabrication route of V_2O_5/C_3N_4 nanocomposites was displayed in Fig. 1. First, 5 g of urea was placed in a covered crucible, and then wrapped with aluminum foil. The crucible was placed in a muffle furnace and heated at a heating rate of 273.5 K·min^{-1} to 823 K for 3 h, cooled naturally to room temperature, and then ground into fine powder. Typically, different amounts of NH_4VO_3 (5 mg, 10 mg, 20 mg, 50 mg) were added into 1 g of the above powder and grounded together with an agate mortar. Afterward, the ground mixed powder was placed in an open crucible for calcination. The open crucible was placed in a muffle furnace and heated at a heating rate of 278 K·min^{-1} to 773 K for 3 h. After cooled naturally to room temperature, and ground to obtain a light-yellow powder of V_2O_5/C_3N_4. According to the expected V_2O_5 contents of V_2O_5/C_3N_4 nanocomposites (0.5 wt%, 1 wt%, 2 wt%, 5 wt%), the obtained samples were denoted as 0.5-VO/CNNS, 1-VO/CNNS, 2-VO/CNNS, 5-VO/CNNS, respectively. Meanwhile, the V_2O_5 contents were determined by ICP measurements, and the results were shown in Table S2. Pure V_2O_5 and ultrathin 2D C_3N_4 nanosheets photocatalyst were synthesized by a similar method without the addition of urea or NH_4VO_3, denoted as VO and CNNS, respectively.

2.3. Details of the activity assessment, characterization and theoretical calculation

Details of the activity assessment, characterization and DFT calculation were presented in the Supporting Information (Table S1. Experimental section).

3. Results and discussion

3.1. Crystal structures and morphologies

The crystal structure, phase purity, and constituents of VO/CNNS nanocomposites were examined by XRD (Fig. 2a). The diffraction peaks of pure VO are indexed as the orthorhombic V_2O_5 structure (JCPDS No. 41-1426) [43], while CNNS are indexed to (100) and (002) diffraction planes of g-C_3N_4 [44]. All VO/CNNS nanocomposites obtain well-defined diffraction peaks for V_2O_5 and C_3N_4 structures, and no impurity phase occurs. The slight red-shift of the (110) facet with the increase in the V_2O_5 amount implied the stronger interplays of components due to the intercalation of V_2O_5. The high-resolution X-ray photoelectron spectra (HR-XPS) also observed similar results.

V 2p peaks (Fig. 2b) for V_2O_5 are fitted into two peaks at binding energies of 524.7 eV and 517.6 eV, ascribed to V $2p_{1/2}$ and V $2p_{3/2}$, respectively [45]. Meanwhile, the V 2p peaks of 5-VO/CNNS shifted to low binding energies compared with 0.5-VO/CNNS, attributed to the stronger interplays with an increased V_2O_5 content. The O 1 s peak (Fig. S1a) of VO and VO/CNNS at 529.9 eV can be ascribed to O^{2-} in the V—O bond [45]. Signals of N 1 s at 401.4 eV could be assigned to C≡N–C in Fig. S1b, and the C 1 s peaks (Fig. S1c) at 281.8 eV and 284.9 eV are assigned to N–C–N coordination in the C_3N_4 phase [46]. Morphological features of 1-VO/CNNS photocatalyst were investigated by SEM imaging. As shown in Fig. 2c, the VO particles intercalated into laminar ultrathin CNNS nanosheets in VO/CNNS composites. The ultrathin 2D nanosheets of CNNS in 1-VO/CNNS were further confirmed by an atomic force microscope (AFM). The thickness of the flat nanosheets is around 1.4 nm as observed in Fig. 2d. In general, V_2O_5 nanoparticles easily agglomerate due to the nanoscale effect, and anchoring the particles onto a substrate improves dispersion [38]. Meanwhile, the ultrathin 2D C_3N_4 nanosheets can serve as a stable substrate that can impede the agglomeration of V_2O_5 nanoparticles and benefit heterojunctions fabrication with abundant coupling heterointerfaces, because of enlarged SSA, amino groups, and positive charges on the surface of 2D C_3N_4 [41,42]. TEM/HRTEM images in Fig. 2e and f clearly distinguish the structures of ultrathin 2D C_3N_4 nanosheets and attached V_2O_5
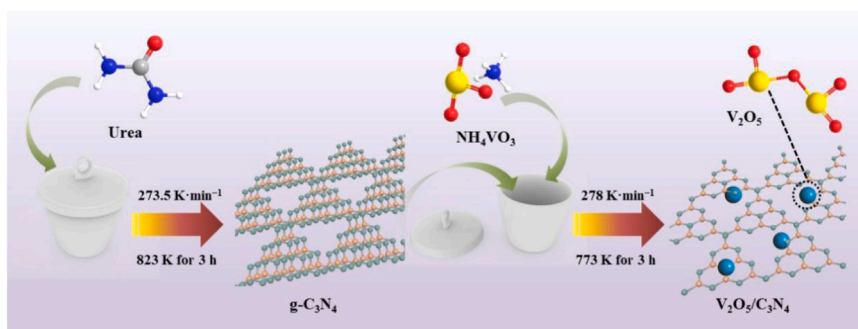
Fig. 1. The fabrication process of VO/CNNS nanocomposites.

nanoparticles. The lattice fringe of 0.341 nm in V_2O_5 assigns to the (110) facet [47], and the lattice fringe of 0.335 nm between the nanosheets corresponds to the (002) facet of 2D C_3N_4 [48]. All these results reveal that V_2O_5 are finely distributed on the surface of ultrathin C_3N_4 nanosheets.

3.2. Photodegradation performance

The photocatalytic activity of the photocatalysts was evaluated for photodegradation of AMX under simulated sunlight. In the absence of catalyst, AMX would not decompose by photolysis under the simulated sunlight (Fig. S2). The as-prepared samples were placed in the AMX solution for 60 min in dark to ensure the adsorption equilibrium (Fig. 3a). The adsorption-desorption equilibrium of all samples was reached within 40 min, and 21.3% of AMX was removed by adsorption with 1-VO/CNNS without light irradiation. The adsorption capacity of VO/CNNS was first improved and then descended with the increased VO content, with is in the same trend with their corresponding SSA (Table S2). The excellent adsorption capacity is beneficial to sufficient contact between AMX and photocatalysts. Notably, the surface atoms released on the interface of VO/CNNS S-scheme heterojunction and abundant nitrogen vacancies derived from CNNS are favorable for the migration of photogenerated e$^-$ and AMX photodegradation [49,50]. Fig. 3a shows that the pure VO and CNNS reach 33.2% and 52.7% of AMX removal under 120 min illumination. All VO/CNNS nanocomposites exhibited significantly enhanced photocatalytic activity than pure VO and CNNS. With the increase of VO loading from 0.5-VO/CNNS to 1-VO/CNNS, the photodegradation efficiency increased from 75.8% to 91.3%. The improved photocatalytic activity of nanocomposites is attributed to the enlarged SSA, increased active sites, and promoted the separation of photoinduced electron-hole pairs by the S-scheme heterojunctions. Besides, further increasing the VO content from 2-VO/CNNS to 5-VO/CNNS inhibited AMX photodegradation from 77.1% to 68.6% accordingly. The reason for decreased photocatalytic activity of 5-VO/CNNS might be that when the VO content is higher than 1 wt%, excessive VO on the surface of CNNS will hinder light absorption of CNNS and cover the active site of CNNS. The kinetics of AMX photodegradation by the as-prepared samples were analyzed in Fig. 3b as first-order reactions. 1-VO/CNNS demonstrates the highest rate constant of 0.0268 min^{-1}, outperforming other photocatalysts in the recent reports (Table S3).

To further investigate the photocatalytic stability and reusability of VO/CNNS nanocomposites, five recycling experiments were implemented by using the spent VO, CNNS and 1-VO/CNNS samples in fresh AMX solutions (Fig. 3c). After five photocatalytic degradation cycles, the activity of pure VO and CNNS notably decreased. However, 1-VO/CNNS only manifests a slight decline in performance. Moreover, XRD tests revealed that the phase and structure of 1-VO/CNNS remain unchanged for the fresh and used samples (Fig. 3d), implying the structural stability of VO/CNNS nanocomposites during photodegradation.

3.3. Investigation on the activities' influence factors

The impacts of initial AMX concentration, photocatalyst dosage, and pH value on this photocatalytic reaction were researched. Photocatalytic degradation with different initial AMX concentrations was shown in Fig. S3a. With the increase of initial AMX concentration from 5 to 40 mg L^{-1}, AMX removal efficiency decreased from 95.6% to 80.7% due to the insufficient reactive species or coverage of active sites by excess AMX molecules [51]. The AMX concentration in factory sewage is about 10–20 mg L^{-1}, while the level is even lower in domestic wastewater [52], suggesting that the as-prepared VO/CNNS exhibited satisfactory photocatalytic performance for removing AMX residual in water environment. As shown in Fig. S3b, the photocatalytic degradation activity of AMX with different 1-VO/CNNS initial dosages was investigated. The photocatalytic degradation activity of AMX increased from 66.2% to 91.3% with the 1-VO/CNNS dosage increased from 0.3 to 0.5 g L^{-1}. However, when 1-VO/CNNS dosage increased to 0.6 g L^{-1}, AMX degradation efficiency decreased to 72.7%. We suppose that when the photocatalyst dosage increases to a certain extent, the transparency of the solution decreased significantly which hindered light penetration and absorption to reach photocatalysts at the bottom level of the solution.

3.4. Photodegradation pathways of AMX

The mineralization of AMX solution was further estimated by the total organic carbon (TOC) tests. Fig. 4a shows the TOC removal in AMX solution during photodegradation with VO, CNNS and 1-VO/CNNS nanocomposite. VO and CNNS reached 19.8% and 31.6% of TOC removal within 120 min, respectively. 1-VO/CNNS nanocomposite attained 76.2% of TOC removal under the same conditions, demonstrating the highest oxidation capacity. In order to investigate the photodegradation intermediates of AMX with VO/CNNS, the solution filtrate was analyzed by high-performance liquid chromatography and mass analysis (HPLC-MS), and the results are displayed in Fig. S4. The main intermediate products of AMX from photodegradation by VO/CNNS are listed in Table S4. Meanwhile, to clarify the photodegradation pathway of AMX, the frontier orbitals and Fuki Index of AMX was computed by density functional theory (DFT). The HOMO and LUMO orbitals of AMX are shown in Fig. 4b and Fig. 4c, revealing that the molecular structure of AMX is totally photostable making it difficult to self-degrade under natural conditions. The DFT calculated the Fukui index describing radical attack (f^0) of the atoms on the AMX molecule (Table S5), and photodegradation pathway of AMX (Fig. 4d) was presented in combination with the detected intermediates by HPLC-MS. The atoms with larger f^0, such as C (2), C (3), O (7), C (19), O (22), and S (25) marked in Table S5, were vulnerable to be attacked by reactive species. The structural formulas of the intermediates have been inferred through their charge-to-mass ratios ($m/z = 117, 133, 149, 165, 192, 201, 216, 232, 247, 324$, and 318), while the m/z value of AMX is 365. AMX molecules and intermediates might be oxidized into other small
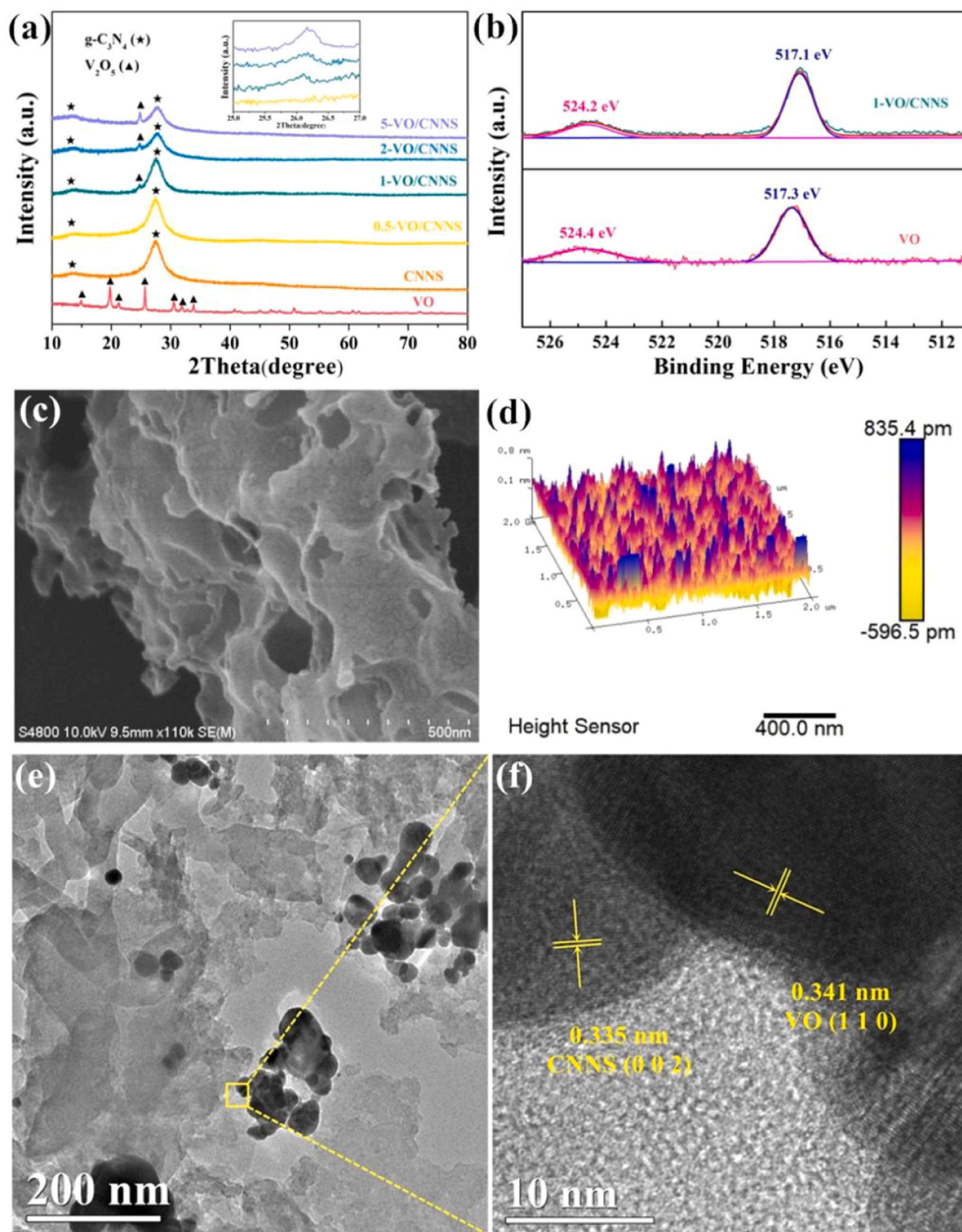
Fig. 2. (a) XRD patterns of the as-prepared VO, CNNS, and VO/CNNS samples, and (b) XPS spectra of V 2p, (c) SEM, (d) AFM, (e) TEM and (f) HRTEM image of 1-VO/CNNS.

molecules and ultimately mineralized into H_2O and CO_2. These results were consistent with TOC analysis. Most of the photodegradation intermediates of AMX are harmless and avirulent [53].

3.5. AMX removal mechanism

The UV–vis diffuse reflectance spectroscopy was tested with VO, CNNS and VO/CNNS nanocomposites, and the results are shown in Fig. 5a. Pure CNNS has an absorption edge at 470 nm, which is

accredited to the quantum confinement effect of CNNS [54]. Pure VO exhibits a sharp absorption edge at about 600 nm, which is ascribed to the narrow band gap of VO in comparison with CNNS. Among all the VO/CNNS photocatalysts, the absorption edge in 470–600 nm range is slightly shifted to longer wavelengths compared with pure CNNS, while the absorption intensities are enhanced with increased VO percentages in VO/CNNS nanocomposites. The all the as-prepared VO/CNNS photocatalysts exhibited broad-spectrum absorption in the sunlight region. Further, the optical band gap energy (*Eg*) of VO, CNNS and as-prepared
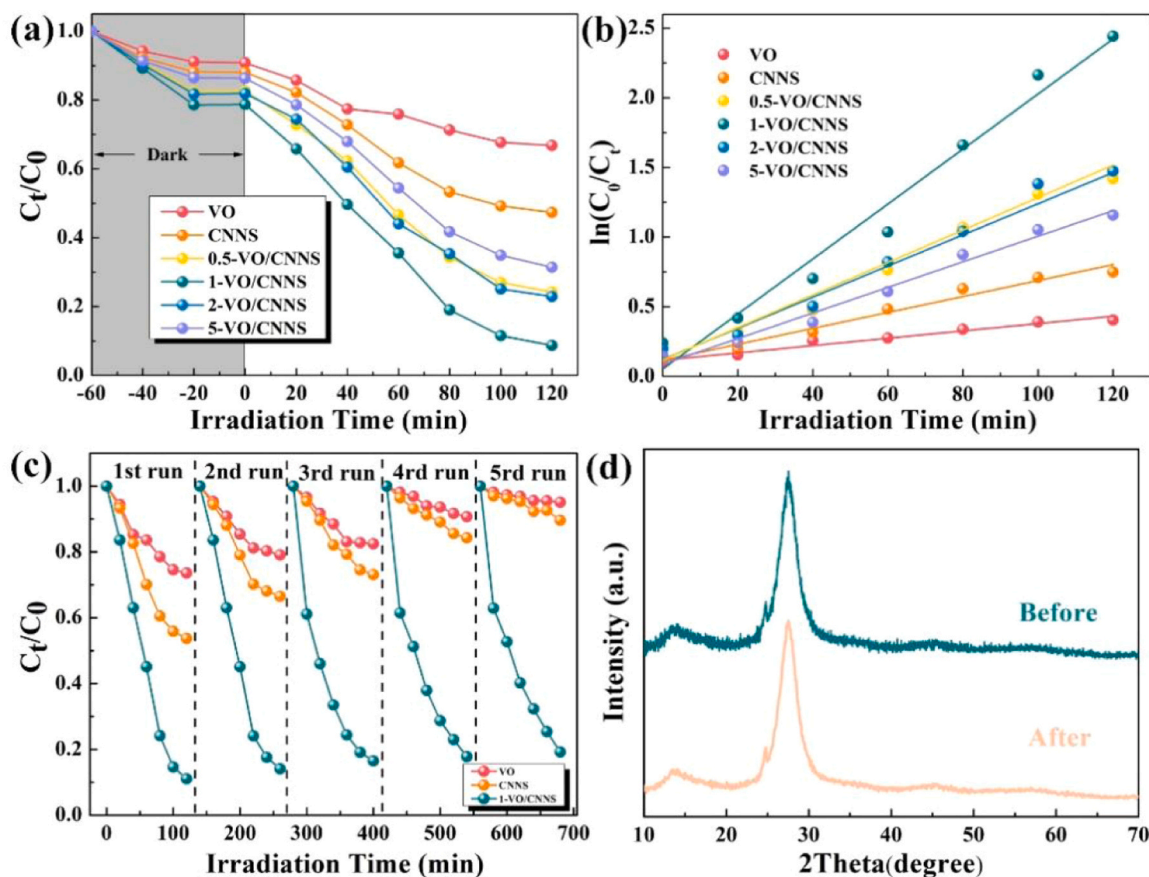
Fig. 3. (a) Photodegradation of the as-prepared VO, CNNS, and VO/CNNS samples and (b) photocatalytic kinetics of different samples; (c) recycling experiments of photodegradation of AMX with VO, CNNS, and 1-VO/CNNS; The initial concentration of AMX solution is 20 mg L^{-1}, the solution pH is neutral, and the photocatalyst dosage is 0.5 g L^{-1}; (d) XRD spectra of 1-VO/CNNS before and after the recycle tests.

VO/CNNS samples can be calculated using the Tauc's plot as shown in Eq. (1) [55]:

$$ahv = A \ (hv - E_g)^{n/2} \tag{1}$$

Among them, α, h, v, A and E_g represent the absorption coefficient, Planck constant, light frequency, proportionality constant related to the material, and band gap energy, respectively. Moreover, n represents the nature of the transition process in the semiconductor (direct transition: $n = 1$; indirect transition: $n = 4$). The n value of VO is 1 [56], and the n value of CNNS is 4 [57]. Thus, the value of the optical band gap of the as-prepared photocatalysts is obtained in Fig. 5b. The corresponding band gap energies of pure VO, CNNS, 0.5-VO/CNNS, 1-VO/CNNS, 2-VO/CNNS, and 5-VO/CNNS samples are 2.21, 2.69, 2.65, 2.61, 2.56, and 2.49 eV, respectively. The increase of VO in the composites leads to a narrow bandgap which responses to the longer wavelength regions and improves photocatalysis under sunlight irradiation.

To further estimated the separation and transfer ability of photogenerated charge carriers, the photoluminescence (PL) spectra of the as-prepared CNNS and VO/CNNS samples were examined in Fig. 5c. To measure the PL emission spectra of the as-prepared samples, 355 nm was set as excitation wavelength. Generally, the higher PL intensity indicates faster recombination of photogenerated carriers, leading to lower photocatalytic activity [58]. The PL intensities of all VO/CNNS samples were obviously lower than pure CNNS, implying that the rapid recombination of photogenerated e$^-$-h$^+$ pairs in CNNS was inhibited after forming the S-scheme heterojunction with VO. The weakest photoluminescence intensity was 1-VO/CNNS among all VO/CNNS nanocomposites, indicating its highest photocatalytic activity.

The transient photocurrent responses of the as-prepared VO, CNNS,

and VO/CNNS samples were tested to characterize the carriers' light response ability. In Fig. 5d, pure CNNS shows lower photocurrent intensity than that of other samples. Moreover, the 1-VO/CNNS exhibit the highest photocurrent intensity compared with other samples, revealing the remarkable separation and migration of photogenerated e$^-$ and h$^+$. Collectively, constructing S-scheme VO/CNNS heterojunctions could enhance the separation of photoinduced charge carriers which is conducive to photocatalysis.

Additionally, the electrochemical impedance spectra (EIS) were tested to investigate the charge transport properties and interface resistance of the as-prepared samples. The smaller the radius of the Nyquist curve in the EIS spectra, the higher separation and migration efficiencies of photogenerated charges. As shown in Fig. 6a, the arc radius of 1-VO/CNNS was smaller than that of CNNS both under dark and light conditions, indicating that loading VO increased the separation efficiency of photogenerated charges of CNNS. Meanwhile, the radius of 1-VO/CNNS under light was smaller than under dark, suggesting that S-scheme heterojunction can improve the photogenerated charge transfer at the VO and CNNS interfaces under sunlight irradiation. The results of PL and EIS analysis jointly confirmed that VO/CNNS has significantly improved charge-transfer efficiency due to the formation of the S-scheme heterojunction.

To determine the main active species in photocatalytic degradation of AMX via VO/CNNS photocatalysts, selective ROS quenching tests were conducted. The results are shown in Fig. 6b. Meanwhile, BuOH (1 mmol), BQ (1 mmol), EDTA (1 mmol), and AgNO$_3$ (1 mmol) are used to capture $^\bullet$OH, O$_2^{\bullet-}$, h$^+$, and e$^-$, respectively [59]. After adding EDTA and BQ, photocatalytic degradation was significantly inhibited, implying that O$_2^{\bullet-}$ and h$^+$ played significant roles in photodegradation
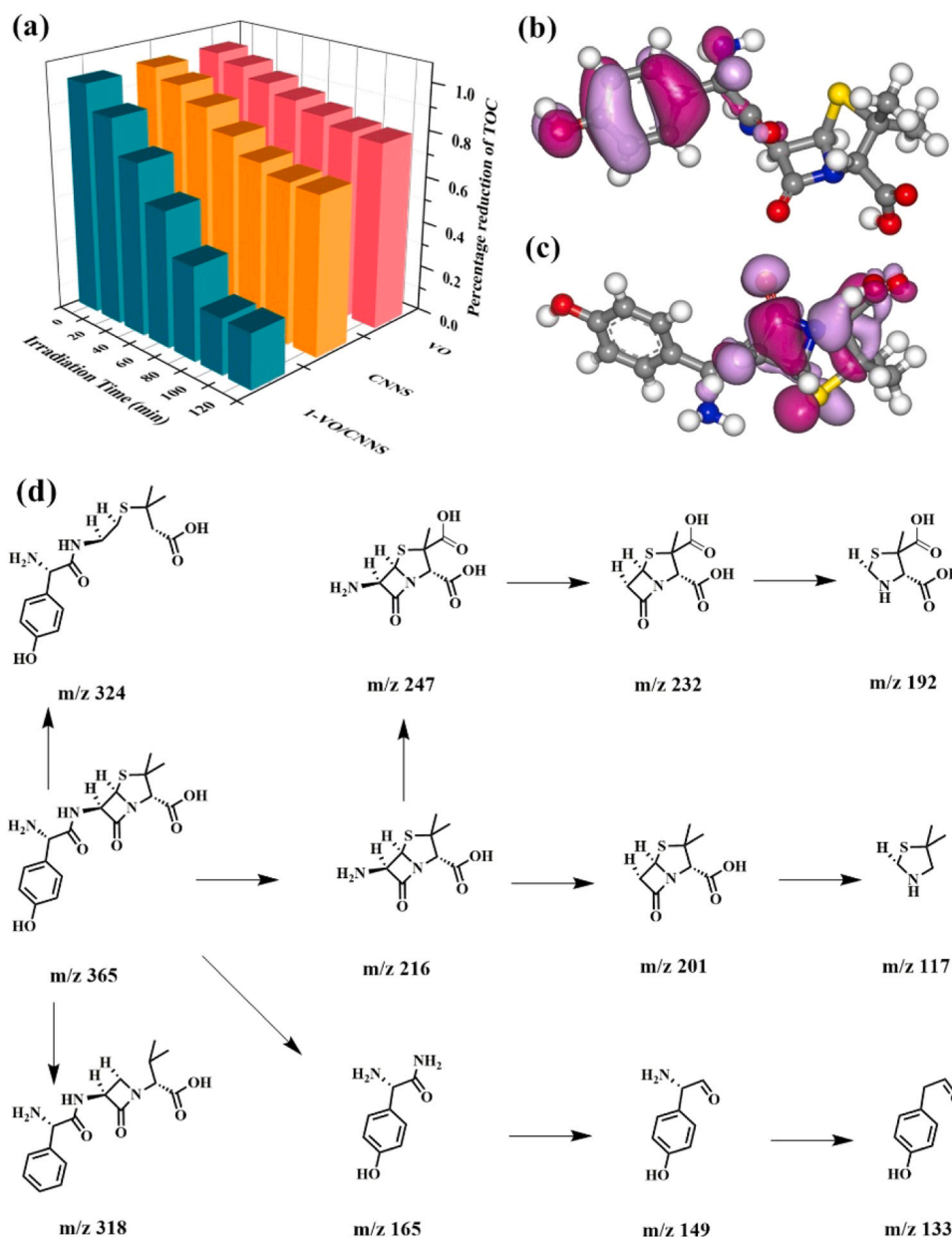
Fig. 4. (a) TOC of AMX solution degraded under different irradiation time by as-prepared VO, CNNS, and 1-VO/CNNS; the (b) HOMO and (c) LUMO orbit images of AMX; (d) the proposed pathways for photodegradation of AMX.

of AMX by VO/CNNS. With the addition of AgNO$_3$, the photocatalytic activity of AMX was slightly reduced because of the inhibited production of O$_2^{\bullet-}$ via DO reduction by photoinduced electrons. However, when BuOH was added, the removal efficiency barely changed, implying that $^{\bullet}$OH was not generated and did not participate in AMX oxidation. Therefore, the primary active species were determined as O$_2^{\bullet-}$ and h$^+$.

To further confirm the active species in the VO/CNNS system, electron spin resonance (ESR) tests were conducted. As shown in Fig. 7a and b under dark conditions, VO/CNNS did not detect typical ESR signals of DMPO−O$_2^{\bullet-}$ and DMPO−$^{\bullet}$OH, indicating that VO/CNNS did not produce O$_2^{\bullet-}$ and $^{\bullet}$OH. Under light irradiation, VO/CNNS exhibited characteristic peaks of DMPO−O$_2^{\bullet-}$ and DMPO−$^{\bullet}$OH. As for CNNS, the ESR signals of DMPO−O$_2^{\bullet-}$ and DMPO− ·OH were also observed (Fig. S5a and b), indicating that O$_2^{\bullet-}$ and $^{\bullet}$OH were produced in the CNNS/photo system. Meanwhile, radical intensities of VO/CNNS are stronger than pure CNNS, implying that more O$_2^{\bullet-}$ and $^{\bullet}$OH were produced in the VO/CNNS photocatalytic system. However, pure VO did not show any

obvious signal in DMPO−O$_2^{\bullet-}$ and DMPO−$^{\bullet}$OH (Fig. S5c and d). Sole VO may not be able to produce radical species. Therefore, the reactive species screening and capturing tests proved that VO/CNNS produces O$_2^{\bullet-}$ and h$^+$ as the main reactive species in photocatalytic oxidation.

To clarify the improved photocatalytic activity of the VO/CNNS composites, the band structures and photodegradation mechanism were investigated. Accordingly, the band edge energy of both CB and VB were calculated according to the Eqs. (2) and (3):

$$E_{CB} = X - E_C - E_g/2 \tag{2}$$

$$E_{VB} = E_{CB} + E_g \tag{3}$$

where X is the Mulliken electronegativity of the constituent atoms; E_C is free electron energy on the hydrogen scale; E_g is the semiconductor band gap energy. Therefore, CB and VB potentials of CNNS are −1.12 and 1.58 eV (vs NHE), respectively, while the CB and VB potentials of VO are 0.50 and 2.71 eV (vs NHE), respectively. Two typical heterojunctions between VO and CNNS are displayed in Fig. 8 to illustrate the
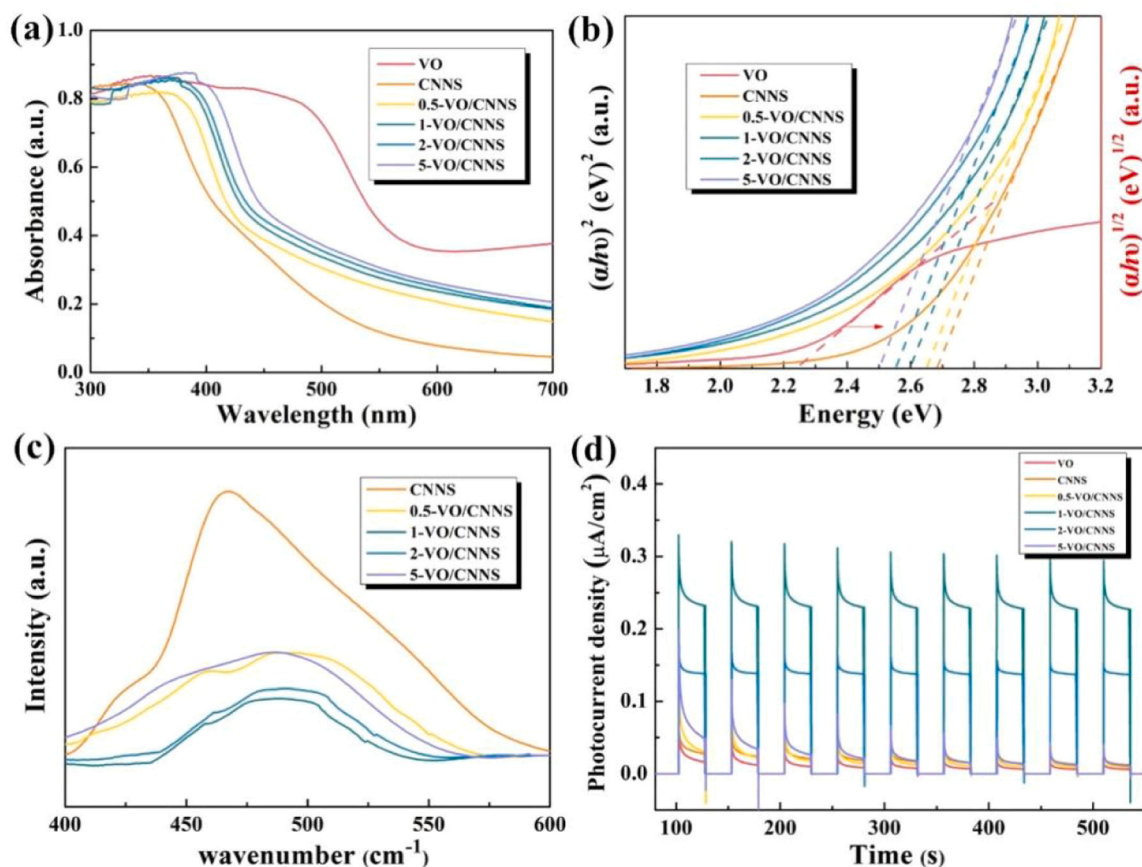
Fig. 5. (a) UV–vis absorption and (b) the band gap energy; (c) photoluminescene spectra and (d) transient photocurrent response of the as-prepared VO, CNNS, and VO/CNNS samples.
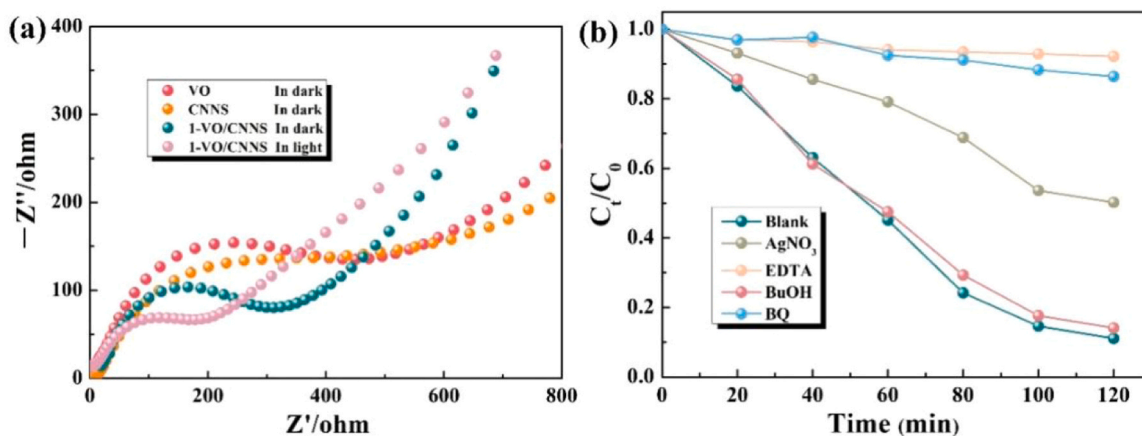

Fig. 6. (a) EIS spectra of as-prepared VO, CNNS, and 1-VO/CNNS samples in dark and under light irradiation. (b) Influence of various scavengers on photocatalytic degradation of AMX with 1-VO/CNNS.

intra-complex charge transfer. In Fig. 8a, the photogenerated e^- from CB of CNNS transfers to CB of VO via the traditional Type II heterojunction, and h^+ migrate from the VB of VO to CNNS. However, $O_2^{\bullet-}$ cannot be produced in this Type II heterojunction because CB of VO is more positive than $O_2/O_2^{\bullet-}$ (−0.33 eV) [60], and $^\bullet OH$ will not be produced because VB of CNNS was more negative than $^\bullet OH /H_2O$ (2.72 eV) [61]. This is contradictory to the ESR findings that both $O_2^{\bullet-}$ and $^\bullet OH$ existed. Thus, we propose an S-scheme mechanism to explain the synergy of the nanocomposites as depicted in Fig. 8b. The VB of VO will up-shifts and CB of CNNS down-shifts to align their Femi levels at the interfaces to form an S-scheme heterojunction. Owing to the differences of Fermi levels and band structures of VO and CNNS, a S-scheme heterojunction is constructed by VO and CNNS as OP and RP, respectively. The photogenerated e^- accumulated on the interface of VO and simultaneously positive charges accumulated on CNNS, leading to the downward band bending of VO and upward band bending of CNNS. Meanwhile, the resulted band bending facilitates the recombination of photogenerated e^- in CB of VO and h^+ in VB of CNNS at the interface. Thus, e^- and h^+ with stronger redox capacities are preserved and will accumulate in the higher CB position of RP (CNNS) and lower VB position of OP (VO),
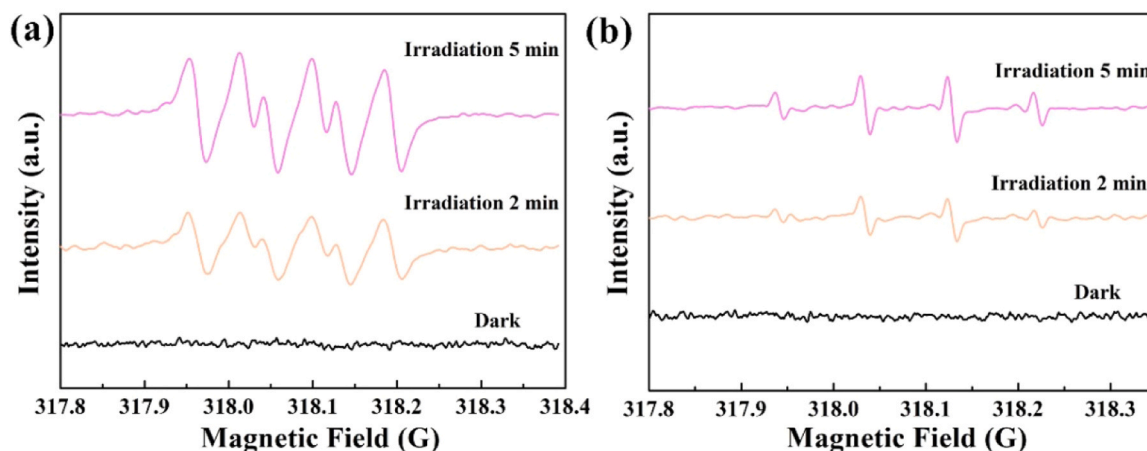
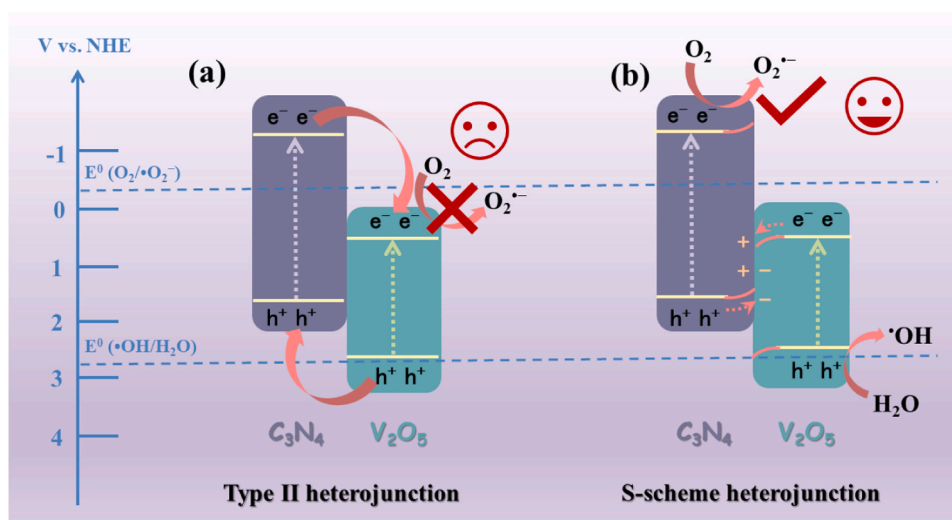**Fig. 7.** ESR spectra of 1-VO/CNNS sample for (a) DMPO$-O_2^{\bullet-}$ and (b) DMPO$-^{\bullet}$OH.

Fig. 8. Mechanism of (a) VO/CNNS type II and (b) S-Scheme heterojunction.

respectively, resulting in the spatial separation of reactive charge carriers for surface reactions. XPS was applied to experimentally identify S-scheme heterojunction. The increase in electron density can be obtained via XPS peaks shifted to lower values. In Fig. 2b, the V 2p of 1-VO/CNNS was shifted to lower values compared with VO, indicating that the electron density increased for V atoms in VO/CNNS. A build-in electric field was established at the VO/CNNS interface owing to the electrons transferred from VO to CNNS. Meanwhile, the photogenerated e^- migrated from CB of VO to VB of CNNS due to the electronic interaction on the VO/CNNS interface. Since the CB edge potential of CNNS (-1.12 eV) is more negative than the potential of $O_2/O_2^{\bullet-}$, photogenerated e^- in the CB of CNNS will reduce O_2 to generate $O_2^{\bullet-}$. Besides, a small part of h^+ with weak oxidation capacity in the VB of VO reacted with H_2O to produce few $^{\bullet}$OH radicals, which were consistent with the ESR results. Meanwhile, the photogenerated h^+ in VO does not produce $^{\bullet}$OH radicals, but directly participates in the photooxidation of AMX.

In summary, loading VO onto ultrathin CNNS nanosheets provides abundant contacted active sites due to the enlarged SSA and intensified the adsorption of AMX on the nanocomposites. After forming an S-scheme heterojunction, photogenerated e^- flows from VO to CNNS until equilibrium, and the spatial separation of the photogenerated e^- and h^+ largely improves the charge separation of each individual component which maintains the active species with strong redox ability. DRS spectra confirmed that VO and CNNS were excited simultaneously to generate photogenerated e^--h^+ pairs under simulated sunlight, which involved into oxidizing species and led to AMX degradation under solar light irradiation. In this S-scheme heterojunction, ultrathin CNNS layers are beneficial to maintaining the structural stability of VO for long-term operation in practical application.

4. Conclusions

An S-scheme heterojunction VO/CNNS photocatalyst was prepared by a simple and convenient heat treatment method, which exhibited excellent activity for photodegradation of AMX residues under simulated sunlight. The VO/CNNS photocatalysts exhibit remarkable reusability in five photodegradation recycles. Characterization techniques revealed the formation of the S-scheme heterojunction structure of VO/CNNS nanocomposite, which enhanced the separation and transfer of photogenerated charge carriers for ROS generation and photocatalytic degradation. The mechanism study signposted that $O_2^{\bullet-}$ and h^+ radicals are the foremost reactive species in photodegradation. This study develops a new S-scheme heterojunction photocatalyst of VO/CNNS for purifying antibiotics pollutants in a high-efficiency and sustainable manner.

CRediT authorship contribution statement

Shukun Le: Conceptualization, Investigation, Visualization, Writing – original draft. **Chengzhang Zhu:** Supervision, Project administration, Writing – review & editing. **Yuwen Cao:** Investigation, Visualization. **Peng Wang:** Investigation. **Quansheng Liu:** Software, Validation, Visualization. **Huacong Zhou:** Investigation, Data curation. **Chuanxiang Chen:** Conceptualization. **Shaobin Wang:** Writing – review & editing. **Xiaoguang Duan:** Supervision, Resources, Project administration, Writing – review & editing.

Declaration of Competing Interest

The authors declare that they have no known competing financial interests or personal relationships that could have appeared to influence the work reported in this paper.

Acknowledgments

Appendix A. Supporting information

Supplementary data associated with this article can be found in the online version at doi:10.1016/j.apcatb.2021.120903.

References

[1] Y. Chen, X. Zhang, L. Wang, X. Cheng, Q. Shang, Rapid removal of phenol/antibiotics in water by Fe-(8-hydroxyquinoline-7-carboxylic)/TiO_2 flower composite: adsorption combined with photocatalysis, Chem. Eng. J. 402 (2020), 126260.

[2] I. Grgic, A.M. Cizmek, S. Babic, D. Ljubas, M. Rozman, UV filters as a driver of the antibiotic pollution in different water matrices, J. Environ. Manag. 289 (2021), 112389, 112389.

[3] M. Chahkandi, M. Zargazi, New water based EPD thin $BiVO_4$ film: effective photocatalytic degradation of Amoxicillin antibiotic, J. Hazard. Mater. 389 (2020), 121850, 121850.

[4] L. Leng, L. Wei, Q. Xiong, S. Xu, W. Li, S. Lv, Q. Lu, L. Wan, Z. Wen, W. Zhou, Use of microalgae based technology for the removal of antibiotics from wastewater: a review, Chemosphere 238 (2020), 124680.

[5] Y. Zhang, X. Xiao, Y. Zhong, T. Lim, Comparison of amoxicillin photodegradation in the UV/H_2O_2 and UV/persulfate systems: reaction kinetics, degradation pathways, and antibacterial activity, Chem. Eng. J. 372 (2019) 420–428.

[6] S. Le, W. Li, Y. Wang, X. Jiang, X. Yang, X. Wang, Carbon dots sensitized ^2D–^2D heterojunction of $BiVO_4/Bi_3TaO_7$ for visible light photocatalytic removal towards the broad-spectrum antibiotics, J. Hazard. Mater. 376 (2019) 1–11.

[7] L. Zhang, S. Du, X. Zhang, G. Lyu, D. Dong, X. Hua, W. Zhang, Z. Guo, Occurrence, distribution, and ecological risk of pharmaceuticals in a seasonally ice-sealed river: from ice formation to melting, J. Hazard. Mater. 389 (2020), 122083, 122083.

[8] S. Liang, X. Hu, H. Xu, Z. Lei, C. Wei, C. Feng, Mechanistic insight into the reaction pathway of peroxomonosulfate-initiated decomplexation of EDTA-Ni-II under alkaline conditions: formation of high-valent Ni intermediate, Appl. Catal. B 296 (2021), 120375, 120375.

[9] Y. Fu, L. Wang, W. Peng, Q. Fan, Q. Li, Y. Dong, Y. Liu, G. Boczkaj, Z. Wang, Enabling simultaneous redox transformation of toxic chromium (VI) and arsenic (III) in aqueous media-a review, J. Hazard. Mater. 417 (2021), 126041.

[10] X. Yang, H. Sun, G. Li, T. An, W. Choi, Fouling of TiO_2 induced by natural organic matters during photocatalytic water treatment: mechanisms and regeneration strategy, Appl. Catal. B 294 (2021), 120252, 120252.

[11] X. Niu, X. Bai, Z. Zhou, J. Wang, Rational design and characterization of direct Z-Scheme photocatalyst for overall water splitting from excited state dynamics simulations, ACS Catal. 10 (2020) 1976–1983.

[12] C. Zhu, Q. Xian, Q. He, C. Chen, W. Zou, S. Wang, X. Duan, Edge-rich bicrystalline $1T/2H-MoS_2$ cocatalyst-decorated {110} terminated CeO_2 nanorods for photocatalytic hydrogen evolution, ACS Appl. Mater. Interfaces 13 (2021) 35818–35827.

[13] Y. Jiang, J. Liao, H. Chen, H. Zhang, J. Li, X. Wang, D. Kuang, All-solid-state Z-scheme alpha-Fe_2O_3/amine-RGO/$CsPbBr_3$ hybrids for visible-light-driven photocatalytic CO_2 reduction, Chem 6 (2020) 766–780.

[14] B. Zhou, S. Ding, Y. Wang, X. Wang, W. Huang, K. Li, G. Huang, Type-II/type-II band alignment to boost spatial charge separation: a case study of g-C_3N_4 quantum

[15] dots/a-TiO_2/r-TiO_2 for highly efficient photocatalytic hydrogen and oxygen evolution, Nanoscale 12 (2020) 6037–6046.

[15] R. Acharya, K. Parida, A review on TiO_2/g-C_3N_4 visible-light-responsive photocatalysts for sustainable energy generation and environmental remediation, J. Environ. Chem. Eng. 8 (2020), 103896, 103896.

[16] Q. Xu, L. Zhang, B. Cheng, J. Fan, J. Yu, S-Scheme heterojunction photocatalyst, Chem 6 (2020) 1543–1559.

[17] C. Cheng, B. He, J. Fan, B. Cheng, S. Cao, J. Yu, An inorganic/organic S-scheme heterojunction H_2-production photocatalyst and its charge transfer mechanism, Adv. Mater. (2021) 2100317.

[18] S. Le, W. Li, Y. Li, B. Borjigin, G. Li, X. Wang, Tetracycline removal under solar illumination over Ag_3VO_4/mpg-C_3N_4 heterojunction photocatalysts, Photochem. Photobiol. 95 (2019) 501–511.

[19] H. Huang, K. Hu, C. Xue, Z. Wang, Z. Fang, L. Zhou, M. Sun, Z. Xu, J. Kou, L. Wang, C. Lu, Metal-free pi-conjugated hybrid g-C_3N_4 with tunable band structure for enhanced visible-light photocatalytic H_2 production, J. Mater. Sci. Technol. 87 (2021) 207–215.

[20] M. Samsudin, H. Ullah, A. Tahir, X. Li, Y. Ng, S. Sufian, Superior photoelectrocatalytic performance of ternary structural $BiVO_4$/GQD/g-C_3N_4 heterojunction, J. Colloid Interface Sci. 586 (2021) 785–796.

[21] Y. Tian, N. Jia, H. Ma, G. Liu, Z. Xiao, Y. Wu, L. Zhou, J. Lei, L. Wang, Y. Liu, J. Zhang, 0D/3D coupling of g-C_3N_4 QDs/hierarchical macro-mesoporous CuO-SiO_2 for high-efficiency norfloxacin removal in photo-Fenton-like processes, J. Hazard. Mater. 419 (2021), 126359, 126359.

[22] Y. Yin, C. Wu, G. Yu, H. Wang, Q. Han, L. Qu, A hierarchical heterojunction polymer aerogel for accelerating charge transfer and separation, J. Mater. Chem. A 9 (2021) 7881–7887.

[23] J. Jia, W. Sun, Q. Zhang, X. Zhang, X. Hu, E. Liu, J. Fan, Inter-plane heterojunctions within 2D/2D $FeSe_2$/g-C_3N_4 nanosheet semiconductors for photocatalytic hydrogen generation, Appl. Catal. B 261 (2020), 118249, 118249.

[24] D. Liu, C. Li, T. Ni, R. Gao, J. Ge, F. Zhang, W. Wu, J. Li, Q. Zhao, 3D interconnected porous g-C_3N_4 hybridized with Fe_2O_3 quantum dots for enhanced photo-Fenton performance, Appl. Surf. Sci. 555 (2021), 149677, 149677.

[25] F. Feng, H. Hua, L. Li, R. Xu, J. Tang, D. Dong, J. Zhang, X. Li, Embedding 1D WO_3 nanotubes into 2D ultrathin porous g-C_3N_4 to improve the stability and efficiency of photocatalytic hydrogen production, ACS Appl. Energy Mater. 4 (2021) 4365–4375.

[26] L. Yu, Z. Mo, X. Zhu, J. Deng, F. Xu, Y. Song, Y. She, H. Li, H. Xu, Construction of 2D/2D Z-scheme MnO_{2-x}/g-C_3N_4 photocatalyst for efficient nitrogen fixation to ammonia, Green Energy Environ. 6 (2021) 538–545.

[27] M. Zhang, C. Lai, B. Li, F. Xu, D. Huang, S. Liu, L. Qin, X. Liu, H. Yi, Y. Fu, Insightful understanding of charge carrier transfer in 2D/2D heterojunction photocatalyst: Ni-Co layered double hydroxides deposited on ornamental g-C_3N_4 ultrathin nanosheet with boosted molecular oxygen activation, Chem. Eng. J. 422 (2021), 130120, 130120.

[28] W. Li, L. Jin, F. Gao, H. Wan, Y. Pu, X. Wei, C. Chen, W. Zou, C. Zhu, L. Dong, Advantageous roles of phosphate decorated octahedral CeO_2 {111}/g-C_3N_4 in boosting photocatalytic CO_2 reduction: charge transfer bridge and Lewis basic site, Appl. Catal. B 294 (2021), 120257, 120257.

[29] W. Li, X. Chu, F. Wang, Y. Dang, X. Liu, X. Wang, C. Wang, Enhanced cocatalyst-support interaction and promoted electron transfer of 3D porous g-C_3N_4/GO-M (Au, Pd, Pt) composite catalysts for hydrogen evolution, Appl. Catal. B 288 (2021), 120034, 120034.

[30] H. Sun, F. Guo, J. Pan, W. Huang, K. Wang, W. Shi, One-pot thermal polymerization route to prepare N-deficient modified g-C_3N_4 for the degradation of tetracycline by the synergistic effect of photocatalysis and persulfate-based advanced oxidation process, Chem. Eng. J. 406 (2021), 126844, 126844.

[31] Y. Wang, L. Liu, T. Ma, Y. Zhang, H. Huang, 2D graphitic carbon nitride for energy conversion and storage, Adv. Funct. Mater. (2021), 120059.

[32] Q. Wang, L. Zhang, Y. Guo, M. Shen, M. Wang, B. Li, J. Shi, Multifunctional 2D porous g-C_3N_4 nanosheets hybridized with 3D hierarchical TiO_2 microflowers for selective dye adsorption, antibiotic degradation and CO_2 reduction, Chem. Eng. J. 396 (2020), 125347, 125347.

[33] G. Di, Z. Zhu, Q. Dai, H. Zhang, X. Shen, Y. Qiu, Y. Huang, J. Yu, D. Yin, S. Küppers, Wavelength-dependent effects of carbon quantum dots on the photocatalytic activity of g-C_3N_4 enabled by LEDs, Chem. Eng. J. 379 (2020), 122296, 122296.

[34] F. Raziq, M. Humayun, A. Ali, T. Wang, A. Khan, Q. Fu, W. Luo, H. Zeng, Z. Zheng, B. Khan, H. Shen, X. Zu, S. Li, L. Qiao, Synthesis of S-doped porous g-C_3N_4 by using ionic liquids and subsequently coupled with Au-TiO_2 for exceptional cocatalyst-free visible-light catalytic activities, Appl. Catal. B Environ. 237 (2018) 1082–1090.

[35] C. Chen, L. Wang, B. Zhu, Z. Zhou, S.I. El-Hout, J. Yang, J. Zhang, 2,5-Furandicarboxylic acid production via catalytic oxidation of 5-hydroxymethylfurfural: catalysts, processes and reaction mechanism, J. Energy Chem. 54 (2021) 528–554.

[36] H. Li, J. Qian, B. Pan, N-coordinated Co containing porous carbon as catalyst with improved dispersity and stability to activate peroxymonosulfate for degradation of organic pollutants, Chem. Eng. J. 403 (2021), 126395, 126395.

[37] Q. Liang, X. Liu, J. Wang, Y. Liu, Z. Liu, L. Tang, B. Shao, W. Zhang, S. Gong, M. Cheng, Q. He, C. Feng, In-situ self-assembly construction of hollow tubular g-C_3N_4 isotype heterojunction for enhanced visible-light photocatalysis: Experiments and theories, J. Hazard. Mater. 401 (2021), 123355, 123355.

[38] C. Liu, R. Li, W. Liu, G. Shen, D. Chen, Chitosan-assisted fabrication of a network C@V_2O_5 cathode for high-performance Zn-Ion batteries, ACS Appl. Mater. Interfaces 13 (2021) 37194–37200.

[39] A. Badreldin, M.D. Imam, Y. Wubulikasimu, K. Elsaid, A.E. Abusrafa, P. B. Balbuena, A. Abdel-Wahab, Surface microenvironment engineering of black V_2O_5 nanostructures for visible light photodegradation of methylene blue, J. Alloy. Compd. 871 (2021), 159615, 159615.

[40] F. Ranjbar, S. Hajati, M. Ghaedi, K. Dashtian, H. Naderi, J. Toth, Highly selective MXene/V_2O_5/CuWO$_4$-based ultra-sensitive room temperature ammonia sensor, J. Hazard. Mater. 416 (2021), 126196.

[41] P. Xia, S. Cao, B. Zhu, M. Liu, M. Shi, J. Yu, Y. Zhang, Designing a 0D/2D S-scheme heterojunction over polymeric carbon nitride for visible-light photocatalytic inactivation of bacteria, Angew. Chem. Int. Ed. 59 (2020) 5218–5225.

[42] V. Balakumar, H. Kim, J.W. Ryu, R. Manivannan, Y.A. Son, Uniform assembly of gold nanoparticles on S-doped g-C$_3$N$_4$ nanocomposite for effective conversion of 4-nitrophenol by catalytic reduction, J. Mater. Sci. Technol. 40 (2020) 176–184.

[43] Z. Lian, J. Wei, W. Shan, Y. Yu, P.M. Radjenovic, H. Zhang, G. He, F. Liu, J. Li, Z. Tian, H. He, Adsorption-induced active vanadium species facilitate excellent performance in low-temperature catalytic NOx abatement, J. Am. Chem. Soc. 143 (2021) 10454–10461.

[44] Y. Li, D. Zhang, J. Fan, Q. Xiang, Highly crystalline carbon nitride hollow spheres with enhanced photocatalytic performance, Chinese, J. Catal. 42 (2021) 627–636.

[45] M. Sribala, B. Meenarathi, V. Parthasarathy, R. Anbarasan, Efficient catalytic activity of novel fluorescent polyimide embedded Ag and V_2O_5 nanoparticles towards the removal of hazardous pollutants, J. Hazard. Mater. 414 (2021), 125606, 125606.

[46] S.J. Lee, T. Begildayeva, H.J. Jung, R. Koutavarapu, Y. Yu, M. Choi, M.Y. Choi, Plasmonic ZnO/Au/g-C$_3$N$_4$ nanocomposites as solar light active photocatalysts for degradation of organic contaminants in wastewater, Chemosphere 263 (2021), 128262, 128262.

[47] I.N. Reddy, V. Manjunath, J. Shim, SnO$_2$ QDs-decorated V_2O_5 nanobelts for photoelectrochemical water splitting under visible light, Ceram. Int. 47 (2021) 21127–21139.

[48] Z. Chen, S. Zhang, Y. Liu, N. Alharbi, S.O. Rabah, S. Wang, X. Wang, Synthesis and fabrication of g-C$_3$N$_4$-based materials and their application in elimination of pollutants, Sci. Total Environ. 731 (2020), 139054, 139054.

[49] J. Jiang, X. Wang, Y. Liu, Y. Ma, T. Li, Y. Lin, T. Xie, S. Dong, Photo-Fenton degradation of emerging pollutants over Fe-POM nanoparticle/porous and ultrathin g-C$_3$N$_4$ nanosheet with rich nitrogen defect: degradation mechanism, pathways, and products toxicity assessment, Appl. Catal. B 278 (2020) 119349, 119349.

[50] J. Cao, W. Nie, L. Huang, Y. Ding, K. Lv, H. Tang, Photocatalytic activation of sulfite by nitrogen vacancy modified graphitic carbon nitride for efficient degradation of carbamazepine, Appl. Catal. B 241 (2019) 18–27.

[51] M. Verma, A.K. Haritash, Photocatalytic degradation of amoxicillin in pharmaceutical wastewater: a potential tool to manage residual antibiotics, Environ. Technol. Innov. 20 (2020) 3683–3692, 101072.

[52] M. Gaeta, G. Sanfilippo, A. Fraix, G. Sortino, M. Barcellona, G.O. Conti, M. E. Fragala, M. Ferrante, R. Purrello, A. D'Urso, Photodegradation of antibiotics by noncovalent porphyrin-functionalized TiO$_2$ in water for the bacterial antibiotic resistance risk management, Int. J. Mol. Sci. 21 (2020) 3775.

[53] M. Chahkandi, M. Zargazi, New water based EPD thin BiVO$_4$ film: effective photocatalytic degradation of amoxicillin antibiotic, J. Hazard. Mater. 389 (2020), 121850, 121850.

[54] F. Nekouei, S. Nekouei, M. Pouzesh, Y. Liu, Porous-CdS/Cu$_2$O/graphitic-C$_3$N$_4$ dual p-n junctions as highly efficient photo/catalysts for degrading ciprofloxacin and generating hydrogen using solar energy, Chem. Eng. J. 385 (2020), 123710, 123710.

[55] S.G. Poulopoulos, G. Ulykbanova, C.J. Philippopoulos, Photochemical mineralization of amoxicillin medicinal product by means of UV, hydrogen peroxide, titanium dioxide and iron, Environ. Technol. 42 (2021) 2941–2949.

[56] J.A. Martin-Martin, M. Gallastegi-Villa, M.P. Gonzalez-Marcos, A. Aranzabal, J. R. Gonzalez-Velasco, Bimodal effect of water on V_2O_5/TiO$_2$ catalysts with different vanadium species in the simultaneous NO reduction and 1,2-dichlorobenzene oxidation, Chem. Eng. J. 417 (2021), 129013, 129013.

[57] D. Kim, K. Yong, Boron doping induced charge transfer switching of a C$_3$N$_4$/ZnO photocatalyst from Z-scheme to type II to enhance photocatalytic hydrogen production, Appl. Catal. B 282 (2021) 119538, 119538.

[58] F. Xu, K. Meng, B. Cheng, S. Wang, J. Xu, J. Yu, Unique S-scheme heterojunctions in self-assembled TiO$_2$/CsPbBr$_3$ hybrids for CO$_2$ photoreduction, Nat. Commun. 11 (2020) 4613.

[59] M.B.R. Kamalam, S.S.R. Inbanathan, K. Sethuraman, A. Umar, H. Algadi, A. A. Ibrahim, Q.I. Rahman, C.S. Garoufalis, S. Baskoutas, Direct sunlight-driven enhanced photocatalytic performance of V_2O_5 nanorods/ graphene oxide nanocomposites for the degradation of Victoria blue dye, Environ. Res. 199 (2021), 111369.

[60] C. Gao, J. Low, R. Long, T. Kong, J. Zhu, Y. Xiong, Heterogeneous single-atom photocatalysts: fundamentals and applications, Chem. Rev. 210 (2020) 12175–12216.

[61] G. Fan, R. Ning, Z. Yan, J. Luo, B. Du, J. Zhan, L. Liu, J. Zhang, Double photoelectron-transfer mechanism in Ag AgCl/WO$_3$/g-C$_3$N$_4$ photocatalyst with enhanced visible-light photocatalytic activity for trimethoprim degradation, J. Hazard. Mater. 403 (2021), 123964, 123964.